Int. J. Electrochem. Sci., 17 **(2022)** Article Number: 220813, doi: 10.20964/2022.08.10

International Journal of
ELECTROCHEMICAL
SCIENCE
www.electrochemsci.org

Vertically Aligned Cu-Doped ZnO Nanorods for Photocatalytic Activity Enhancement

J. Ridwan [1], J. Yunas [1,], A.A. Umar [1], A.A. Mohd Raub [1], A.A. Hamzah [1], J. Kazmi[1]*
A.B.D. Nandiyanto [2], R.E. Pawinanto [2], and I. Hamidah [2]

[1] Institute of Microengineering and Nanoelectronics, Universiti Kebangsaan Malaysia, 43600, UKM-Bangi, Selangor Malaysia
[2] Faculty of Engineering Education, Universitas Pendidikan Indonesia, Jl. Dr. Setiabudhi 207, Bandung 40154, Indonesia.
[*]E-mail: jumrilyunas@ukm.edu.my

Received: 8 April 2022 / *Accepted:* 17 May 2022 / *Published:* 4 July 2022

This paper reports the synthesis and characterization of Cu-doped ZnO nanorods with enhanced photocatalytic activity in degrading industrial wastewater contaminations. Arrays of the doped nanorods are grown in the precursor solution using a hydrothermal process at various growth durations and Cu contents (1% to 15% mol). Results of the synthesis process are analyzed using finite element scanning electron microscopy (FESEM), energy dispersive X-ray analysis (EDAX), X-ray diffraction (XRD), and Raman spectroscopy. The optical properties of the photocatalyst are analyzed using photoluminescence and UV-Vis analyses. EDAX spectra of the synthesized nanorods confirm the presence of Zn, O, and Cu. The XRD patterns show the typical hexagonal ZnO in the (0 0 2) plane. Meanwhile, FESEM images show the vertically aligned nanorods in which the geometries of the structure depend on the growth time. In addition, Cu doping on ZnO affects the physical dimension of the rod structure and the optical properties of the ZnO nanorods. Compared with pristine ZnO, the ZnO/Cu nanorods have approximately 44% shorter length and approximately 36% higher diameter. The Cu doping also enables photon absorption in the visible light spectrum to improve photocatalytic activity. Photocatalytic degradation test results show that the highest methylene blue reduction of 97% is obtained using ZnO nanorods doped with 4 mol% Cu under 30 W UV exposure. The developed photocatalyst system could improve human health and environmental quality.

Keywords: Cu doped ZnO, nanorods; photocatalyst; hydrothermal; methylene blue degradation.

1. INTRODUCTION

Many industries, such as textile, printing, pharmaceutical, leather, food, and cosmetics, discharge approximately 10%–15% of synthetic dyes as waste products in open areas, such as rivers, lakes, and

landfills. This large amount of liquid waste contains toxic compounds that exert harmful effects, such as hemorrhage, skin irritation, nausea, and skin ulceration, on humans and cause environmental pollution [1-3]. As an example, processing 12–20 tons of textiles releases approximately 1000–3000 m^3 of effluents every day, and this waste contains high concentrations of dyes, such as methylene blue (MB) and methyl orange, and various metals, such as Cd, Cr, Pb, and Ni [4, 5].

Industrial wastewaters have been treated using chemical approaches, including active carbon adsorption [6, 7], chemical precipitation and separation [8], and coagulation [9]. However, these methods cannot destroy the chemical bond of organic contaminants completely. In addition, the undegraded products would be transformed into another contaminations phase and require posttreatment processes. This phenomenon increases the process cost in degrading industrial contaminants [10]. Advanced oxidation through the photocatalytic process are an effective alternative. This approach can mineralize the organic contaminants present in wastewater and destroy the complex structure using short-lived, highly oxidizing chemical species through the photochemical process [11].

Some metal oxide semiconductor materials, including ZnO, TiO_2, SnO_2, In_2O_3, WO_3, and Fe_2O_3, have been investigated and used for various optoelectronic applications, especially as photocatalysts [12-15]. Among those materials, ZnO semiconductors have better efficiency in degrading organic contaminants than other metal oxides because of their wide direct bandgap, room-temperature photoinduced electron–hole pairs, large exciton binding energy of approximately 60 meV at 300 K, and excellent chemical and thermal stabilities [16, 17]. Table 1 shows the current ZnO photocatalyst performances and their implementation in MB degradation.

Table 1. Photocatalytic performance of ZnO-based photocatalysts.

Material	Eg [eV]	Contaminant	Photocatalytic performance	Reference
Fe–ZnO nanoparticles	3.2-3.37 eV	Methylene blue (MB),	86%, 92%	[18]
ZnO nanowire	3.2-3.37 eV	Methylene blue (MB),	10%	[19]
ZnO nanoparticles	2.2 - 2.9 eV	Methylene orenge, Methylene blue (MB),	50% 15% ~27%	[20]

ZnO in the form of nanoparticles has several advantages, such as high surface reactivity to increase efficiency in generating hydroxyl ions and strong oxidation power to degrade organic compounds under UV irradiation [21]. However, the main drawbacks of the nanoparticles are particle agglomeration due to particles floating in the solution during the photocatalytic reaction and the requirement for a separation process between wastewater and ZnO nanoparticles. The low photocatalytic activity of ZnO as the turbid wastewater and the complex method of filtration of nanosized inorganic particles limit the photocatalytic efficiency during aqueous-phase pollutant degradation on an industrial

scale [22]. Furthermore, nanoparticle photocatalysts cause secondary pollutants and transform into other carcinogenic, mutagenic, and toxic compounds after degradation [23].

These problems have encouraged researchers to build robust, stable, and reproducible photocatalytic processes by implementing static ZnO nanorod (NR) structures [24]. In addition, the efficiency of metal–semiconductor photocatalysis can be further improved by modifying the material's properties through doping, which increases absorption at a broad wavelength spectrum range, improves electron transfer by promoting the effective generation of electron–hole pairs, and reduces electron–hole recombination [25, 26].

Some other researchers have implemented doping using rare-earth ions [27], transition metals such as Ag-ZnO [28, 29], Au-ZnO [30, 31], Al-ZnO [32-34], and ZnO coupled with other metal oxides (e.g., ZnO-TiO2 and ZnO-SnO2) [12, 13, 35]. The material modifications improve the device in various applications, such as gas sensors [36], light-emitting diodes [37], solar cells [30, 38], nanogenerators [39], and field-effect transistors [40].

In the present study, ZnO NRs were synthesized using the hydrothermal method, which is simple, cost efficient, and allows flexible morphology control [41]. The synthesized ZnO/Cu NRs were characterized, and the effect of Cu doping on the ZnO NRs in degrading organic contaminants was analyzed. The doping was aimed at reducing the bandgap and enlarging the light spectrum. Cu as a dopant to ZnO was used because of its advantages, including excellent optical properties, in the green emission band, which can activate ZnO NRs within the visible range spectrum [42, 43]. Moreover, the atomic radius of Cu2+ closely matches with that of Zn2+, which makes it easy to substitute to the ZnO lattice [44]. Incorporating Cu in ZnO enhances the photogeneration of electron–hole pairs and effectively inhibits the electron–hole recombination to improve the photocatalytic effect of the NRs. [45-47]. Meanwhile, implementing the static NRs would increase the light absorption capability with recyclability for repeatable photocatalysis.

2. MATERIALS AND METHODS

2.1. Material Preparations

ZnO/Cu NRs were synthesized using a hydrothermal process. Glass slides served as the substrate. Analytical reagents, such as ZnAce dehydrate (Zn(CH3COO)2·2H2O, methanol, and NaOH, were used as precursor sources to prepare the seed layers. Hexamethylenetetramine (HMTA; C6H12N4), zinc nitrate hexahydrate (Zn(NO3)2·6H2O), and copper nitrate powders $Cu(NO_3)2$ were used to grow ZnO NRs. MB solution was used as the contaminant sample.

2.2. Synthesis of ZnO NRs

Figure 1 shows the schematic of the process flow, and Table 2 lists the synthesis parameters investigated, included doping composition and growth time, which exert the most significant effects on the NRs as previously reported [48, 49].

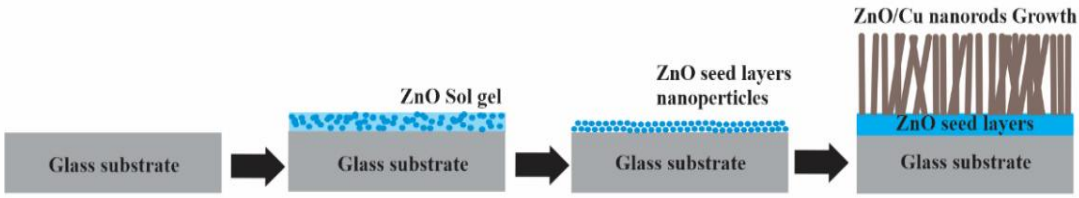

Figure 1. Schematic of ZnO/Cu NR growth.

The process was mainly conducted in three phases, including the dispersion of ZnO nanoparticles using the solgel process, the seeding of nanoparticles, and the growth of NRs. The process started with substrate cleaning in deionized (DI) water and ethanolic solution using an ultrasonic bath for 15 min at 50 °C. The sol–gel was prepared with 10 mM ZnAc and then stirred at 60 °C with a speed of 600 rpm for 30 min. Meanwhile, a 10 mM NaOH diluted in methanol solution was prepared in another beaker glass. Then, the sodium hydroxide was dropped and mixed with the precursor solution of ZnAc to reach pH 11 until the solution gradually turned from clear to a milky solution. Finally, the mixed solution was stirred for another 2 h to form a clear and homogeneous solution. The detailed description to grow ZnO NRs can be referred in our previous work [50].

Table 2. Hydrothermal growth parameters of ZnO/Cu nanorods.

Process sequence	Chemical solution	Cu composition in precursor [%mol]	Growing temperature [°C]	Growing time [h]	Annealing
ZnO sol-gel preparation	Zn(CH3COO)2 2H2O Methanol (NaOH)	N/A	N/A	N/A	N/A
Seed layer coating	ZnO sol-gel nanoparticle solution	N/A	N/A	N/A	350 °C, 1 h
ZnO growth with Cu Doping	C6H12N4 (HMTA) Zn(NO3)2·6H2O) $Cu(NO_3)2$ powder	0 (no doping) 1; 2; 3; 4; 5; 10; 15	90 °C	2; 3; 6	350 °C, 1 h

The following process is the coating of the seed layer using a spin coater. In this process, 50 µl of THE prepared sol–gel was dropped on top of a cleaned glass substrate with a speed coating of 3000 rpm for 30 s. The coated substrate was then placed on a hot plate at 100 °C for 10 min. This process was repeated for the dense and homogeneous nanoparticle distribution on the substrate surface followed by annealing in the furnace at 350 °C for 1 h.

The final step of the synthesis process was the hydrothermal growth of Cu-doped ZnO NRs. The growth of ZnO NRs started by mixing 25 mM zinc nitrate with the equimolar of HMTA in DI water. This precursor solution was mixed using a magnetic stirrer at 60 °C with a rotation speed of 600 rpm for 1 h. Then, the Cu-doped ZnO NRs were grown by mixing zinc nitrate (25 mM) with the equimolar of HMTA and $Cu(NO_3)2$ powder with Cu composition in the precursor solution by molarity ratios ranging

from 1% to 15% mol. Subsequently, this solution was transferred onto a pre-coated substrate followed by a growth process at 90 °C in an electric oven (Memmert Steriliser SN30, Germany) for 2, 3, and 6 h. In addition, Cu-doped ZnO NRs were grown for 6 h. Then, the grown ZnO NRs in the substrate were washed using DI water to remove the excess salt and residues. Finally, the ZnO NRs were annealed in the furnace (Thermcraft Inc. Winston-Salem, NC) at 350 °C in ambient air for 1 h to remove organic contaminants.

2.3. Characterization and Photocatalyst Test Setup

In this study, the morphology and structure of the synthesized NRs were studied using a Merlin field-emission electron microscope (FESEM). ZnO/Cu content was detected using energy dispersive X-ray (EDAX) spectroscopy, and X-ray diffraction (XRD) was used to study the crystallography structure of ZnO/Cu. A Raman spectrometer with a laser power of 3.5 mW was also used to examine the crystallinity of the NRs, whereas the photoluminescence of ZnO/Cu was measured using a PL spectrometer (Edinburgh Instrument FLS920). The optical absorption spectra of the samples were analyzed in the optical wavelength range of 350–800 nm using a UV-Visible spectrometer.

The functionality of the synthesized NRs was tested. The photocatalytic study of Cu-doped ZnO NRs and pristine ZnO NRs was performed by monitoring the degradation of MB under UV light illumination (18 W, 3 h). In this photodegradation test, the synthesized NRs on a glass substrate were placed in 5 mL of 0.05 mM MB solution. The sample substrates include the pristine ZnO and Cu-doped ZnO.

Photocatalytic activity tests of the undoped and Cu-doped ZnO NRs were run three times to study the stability of the synthesized photocatalyst and the durability of the nanostructure's adhesion on glass substrate after immersing in the solution for a long period.

3. RESULTS AND DISCUSSION

3.1. FESEM Analysis

Figure 2 shows the FESEM results of the initial ZnO NRs grown without any doping. The growth times were varied (2, 3, and 6 h) with a constant growth temperature of 90 °C. The NR structure grew in a vertical direction with a slightly tilted orientation because of the quality of the glass surface and the homogeneity of the dispersed nanoparticles on the seed layer. The grown NRs had a hexagonal crystal structure, which met the ZnO crystal specification reported previously [51]. Figure 2(a,d,g) shows the top view of the ZnO NRs, revealing that rod diameters within the range of 20–90 nm were obtained. For growth time at 6 h, the maximum NR diameter of 64 nm was observed. As shown in Figure 2(c,f,i), the size-frequency distribution of the ZnO NRs diameter increased with increasing growth duration.

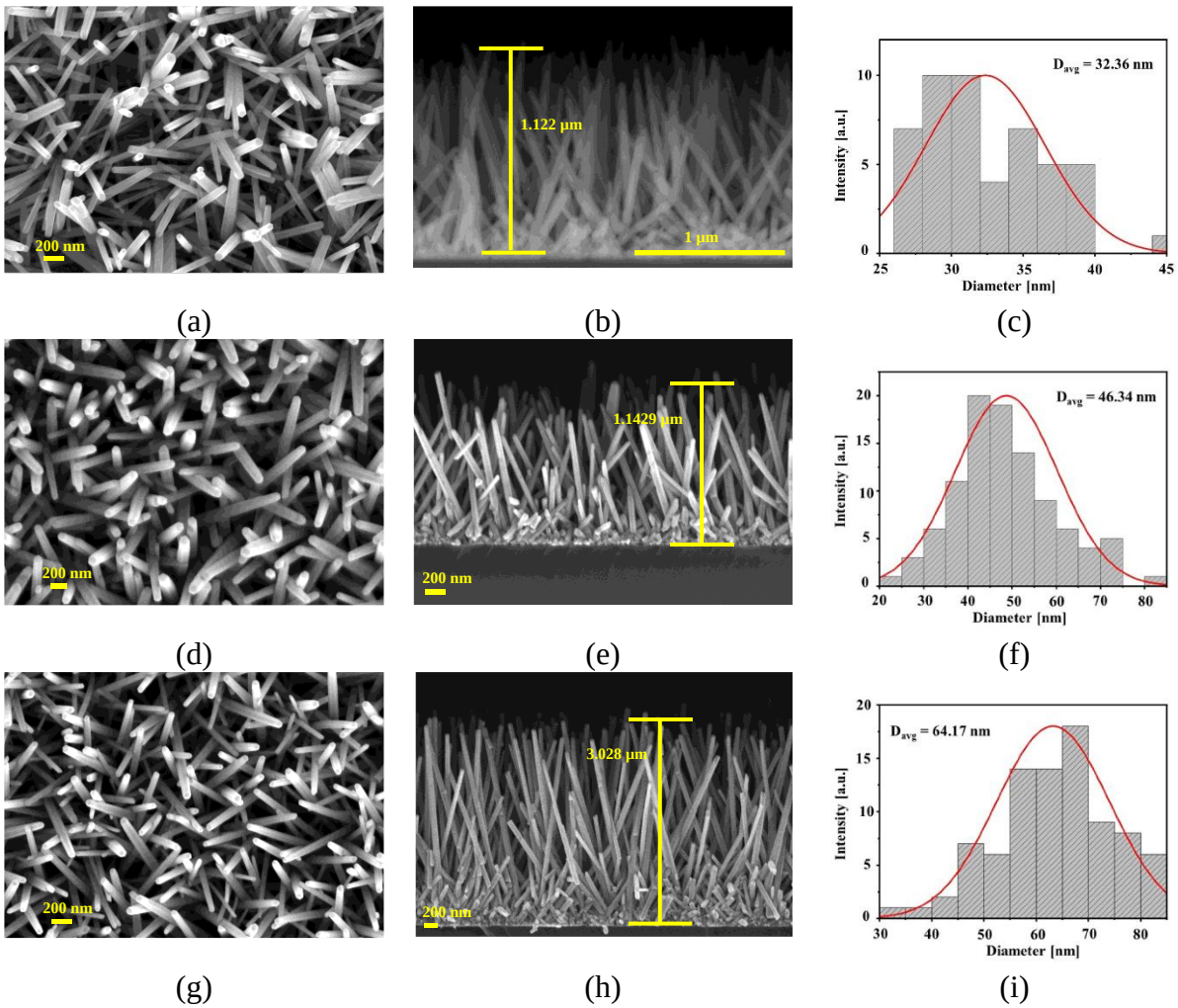

Figure 2. FESEM photographs of the top view with a cross-sectional view and diameter size of undoped ZnO nanorods grown at 90 °C, (a,b,c) for 2 h, (d,e,f) for 3 h, and (g,h,i) for 6 h.

Meanwhile, the length of the grown ZnO NRs increased with increasing growth duration, as shown in Figure 2(b,e,h). The length of the grown NRs doubled in size when the growth time doubled, which were 1.266 and 3.028 µm for 3 and 6 h growth, respectively.

Figure 3 shows the FESEM results for ZnO grown with Cu doping. Our initial analysis was performed on the ZnO samples grown with Cu at 4%, 5%, and 15% compositions at the growth temperature of 90 °C for 6 h. Cu doping significantly affected the physical structure of the NRs. The diameter of ZnO NRs increased with increasing copper composition. The diameter increased from 60 nm to average 90 nm for the pristine ZnO NRs and Cu-doped ZnO NRs, respectively. Meanwhile, Figures 3(b,e,h) shows that the length of the Cu-doped ZnO NRs decreased with increasing Cu content in the precursor.

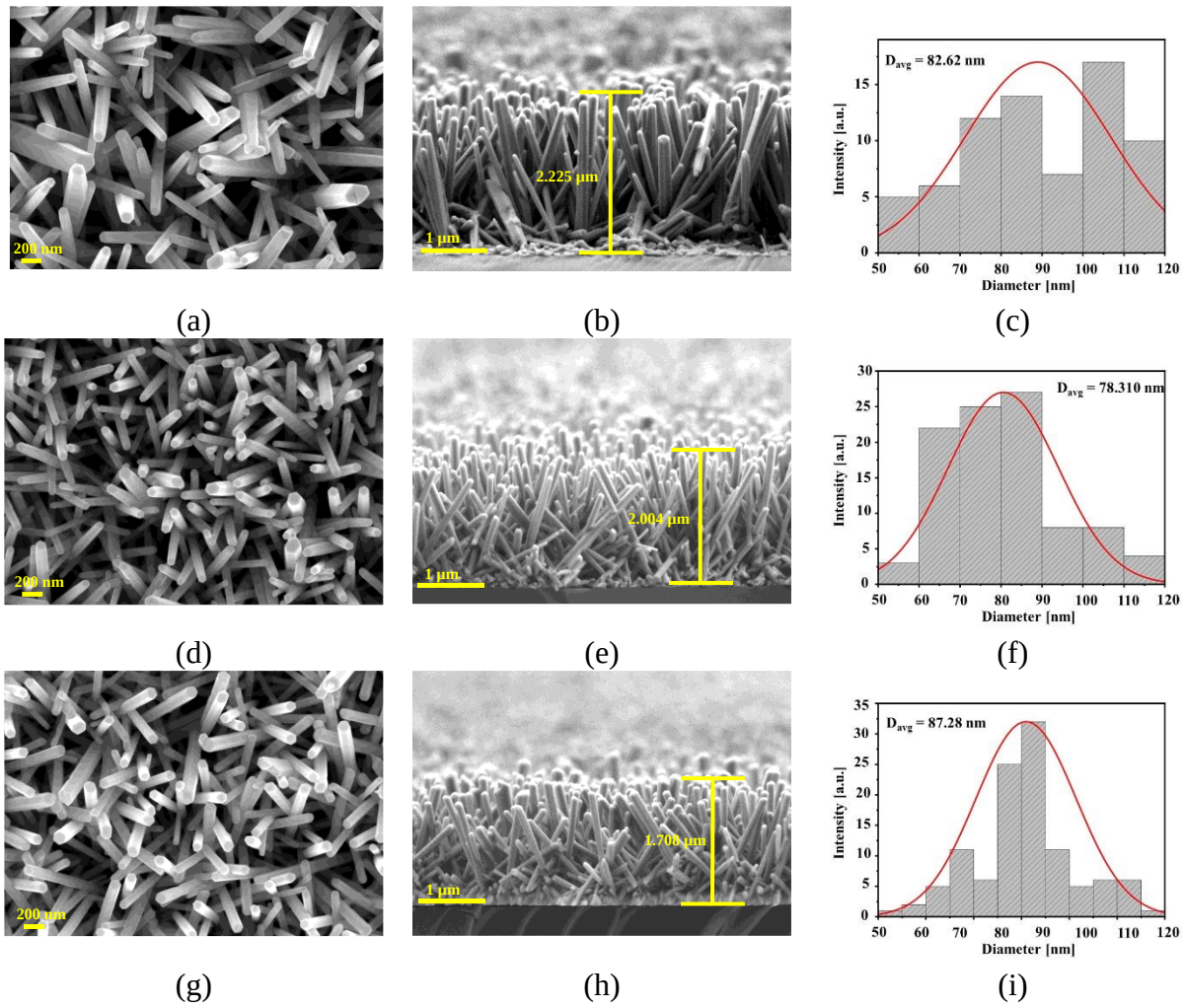

Figure 3. FESEM images of top view with cross-sectional and size distribution of grown view of grown ZnO nanorods with Cu precursor composition of 4 mol% (a,b,c), 5 mol% (d,e,f), and 15 mol% (g,h,i) at the growth temperature of 90 °C for 6 h.

In addition, Figure 3(g,h,i) shows that the diameter and length ZnO grown for 6 h with 15% Cu in the precursor considerably differed with the undoped ZnO. The length of ZnO doped with 15 mol% Cu in the precursor was approximately 1.7 µm (Figure 3h), which was 44% shorter than that of pristine ZnO (Figure 2h). The average diameter distribution was observed at approximately 87 nm (Figure 3i), which was approximately 36% higher than that of pristine ZnO (Figure 2i). The results indicated that the incorporation of Cu into ZnO NRs affected the dimension of the grown structure.

The length of the NRs plays an essential role in photon absorption capability. The optimum length and diameter of the rod structure are preferred to enhance photocatalytic activity. A long and large NR structure prevents light penetration, reducing the accident light on the surface [28] and exhibiting the contaminant reaction with the photocatalyst [52, 53].

3.2. EDAX and XRD Analyses

Figure 4 shows the EDAX analysis of the initial Cu-doped ZnO NRs, confirming the presence of ZnO and Cu. The two highest peaks belonging to Zn and O and the existence of Cu occupied a small portion in the EDAX spectrum. The chemical composition of the Cu-doped ZnO NRs is shown in Figure 4(a,b, and c), which indicates the presence of Cu doped in the ZnO at 0.7, 1.3, and 2.8 wt% for the sample prepared using Cu precursor solutions at 4%, 5%, and 15% mol, respectively. This result indicates that the composition of Cu doped in ZnO NRs increased with the Cu amount in the precursor solution.

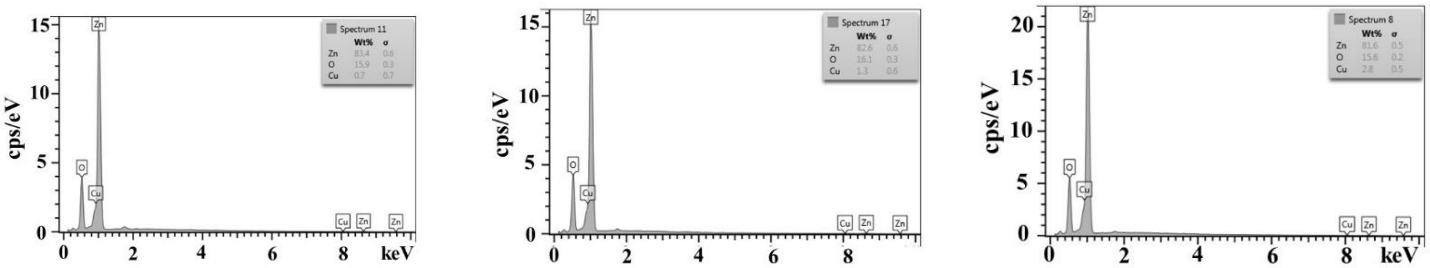

(a) (b) (c)

Figure 4. EDAX results of (a) ZnO with Cu composition in the precursor of 4 mol% at 6 h growth, (e) ZnO with Cu composition in the precursor of 5 mol% at 6 h growth, and (f) ZnO with Cu composition in the precursor of 15 mol% at 6 h growth.

Figure 5(a) shows the XRD patterns of pristine ZnO (undoped) and ZnO/Cu NRs, which reveals the main peak of the samples at (1 0 0), (0 0 2), and (1 0 1). The analysis result indicates the hexagonal structure of ZnO. The sharp peak in the (0 0 2) plane indicated that the ZnO NRs samples grew perpendicular to the glass substrate and achieved a good crystal quality [54].

Moreover, no copper peak was found in the XRD pattern detected, indicating that the doping of Cu into the ZnO NR lattice did not change the ZnO crystalline structure [55]. The intensity of the peak indexed to the (0 0 2) plane decreased with the increase in Cu content. In addition, the peak in (0 0 2) shifted to a higher angle as the Cu content in ZnO was increased. This result can be ascribed to the extrinsic doping of ZnO in the crystal strain [54, 56].

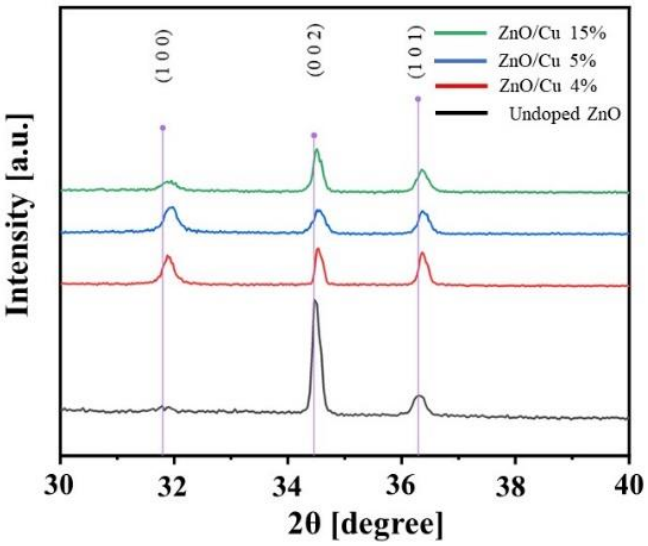

Figure 5. XRD pattern of grown ZnO when doped with copper

3.3. Raman Analysis

Figure 6 shows the structure crystallinity of ZnO NRs on glass substrates analyzed using the typical Raman scattering. Initially, the undoped samples grew at various durations (2, 3, and 6 h), as shown in Figure 6(a). Then, the ZnO samples grown for 6 h with Cu composition from 5 mol% up to 15 mol% in precursor solution were studied using Raman spectroscopy, as shown in Figure 6(b). Theoretically, the Brillouin zone with six active optical phonon modes of ZnO provides information about the crystalline structure of grown ZnO NRs [57]:

$$\Gamma_{opt} = E2_L + E2_H + A1_T + A1_L + E1_T + E1_L, \quad (4)$$

where $E2_H$ and $E2_L$ represent the sublattice vibration of Zn and O atoms, respectively.

Initial analysis on the undoped ZnO in Figure 6(a) shows two major peaks E2 (high) and E2 (low) linked to the vibration of the heavy Zn sublattice and the oxygen atoms, respectively. These two nonpolar components associated with the low frequency of the LO and transverse optical components of different frequencies are part of the two polar branches A1 and E1, respectively [57]. The dominant and sharp peaks at approximately 96 and 433 cm^{-1} were observed, which corresponded to the intrinsic characteristics of the Raman active E2 (low) and E2 (high) modes of the hexagonal wurtzite ZnO. The sample exhibited the Raman active E2 (high) phonon mode at 433 cm^{-1}, which shifted to approximately 4 cm^{-1} compared with the standard E2 (high) phonon mode in the standard ZnO dataset (437 cm^{-1}). This shift can be attributed to the compressive stress in the ZnO NR sample, which causes oxygen vibration [58].

Raman spectra in Figure 6(a) revealed that the Raman intensity increased with prolonged growth time. Moreover, Cu doping into ZnO NRs affected not only the intensity but also the shifting of the Raman active mode, as represented in Figure 6(b). The Cu doping contributed to the diameter change of ZnO NRs, thereby confirming the FESEM image in Figure 3. The Raman intensity increased

significantly with increasing Cu doping concentration because of the change in NR size [59, 60]. Moreover, the Raman peaks shifted slightly from 433 cm^{-1} to 435 cm^{-1} for the undoped ZnO NRs and ZnO/Cu NRs, respectively. This shift in peaks toward a higher wavenumber in the Raman spectra can be ascribed to the strain of the crystal lattice. Thus, Cu changed the chemical bond length in the ZnO lattice. This result indicates the successful Cu incorporation into ZnO NRs [61]. No Raman peaks of CuO or Cu2O appeared in the spectrum. Cu doping did not change the crystal structure of ZnO NRs [62, 63].

The peaks related to Raman active phonon modes were observed as second-order and A1(TO) at approximately 330 and 380 cm^{-1}, respectively [64]. In addition, other peaks were detected at ~586 cm^{-1}, which was linked to E1(LO) when Cu was doped into ZnO NRs, because of defects such as oxygen vacancies and resonance combination of zinc atoms in the ZnO crystal lattice at the excitation wavelength [58].

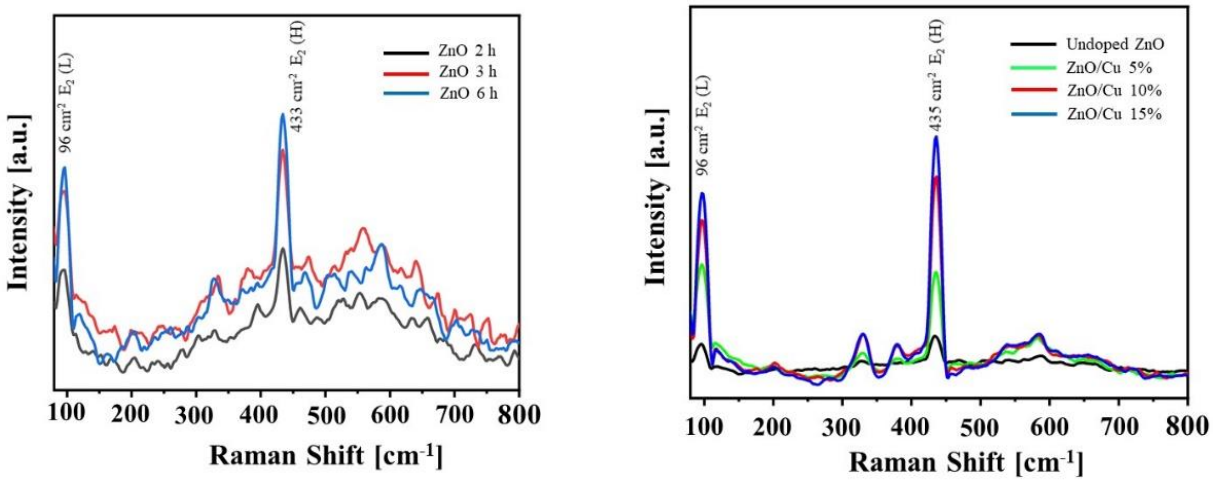

Figure 6. Room-temperature Raman spectra (a) of the as-grown ZnO NRs various growing duration, and (b) ZnO with Cu composition in precursor of 5, 10, and 15 mol% grown for 6 h.

3.4. Optical Property Analysis

The optical properties of the synthesized NRs were initially studied using PL spectroscopy. Initially, the Cu-doped ZnO NRs with Cu content varying from 5 to 15 mol% were taken for analysis. Figure 7 shows the PL spectra of the ZnO/Cu NRs measured within the 350–800 nm wavelength range. Cu doping into ZnO with different concentrations affected the luminescence spectra. The luminescence intensity of the doped ZnO samples was higher at all visible light spectra than the undoped ZnO. The higher intensity was due to the different volume-to-diameter ratios of grown ZnO NR structures and other factors, such as donor–acceptor pair transition, doping defect state, zinc interstitial, and oxygen vacancy [65, 66].

The spectra peak in the UV range presented in this result was approximately ~398 nm, which is known as exciton recombination due to the transition of the donor–acceptor pair. The other peaks observed in a broad visible optical spectrum at approximately 465 nm (deep-level emission or blue emission band), 520 nm (green emission band), 604 nm (orange emission band) were caused by the recombination of the electrons with a deeply trapped hole in the oxygen vacancy or can be linked to zinc ions of ZnO nanomaterials [17, 67]. Cu2+ affects the internal structure of the zinc site and induces more defect states or deep trap energy levels between valence and conduction bands [68, 69]. Moreover, the PL intensities of the green and orange emission bands for undoped ZnO NRs are still considered high because of the more surface oxygen vacancies of the ZnO NRs [70].

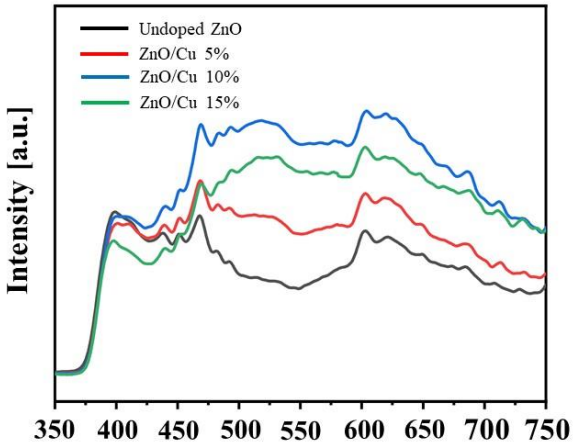

Figure 7. PL spectra of undoped ZnO nanorods, ZnO with Cu composition in precursor of 5%, 10%, and 15% mol.

To study further the effect of the Cu composition on the optical property of the ZnO NRs, the sample specification to be analyzed was extended with smaller Cu contents varying from varied from 1 up to 5 mol% Cu and measured using UV-Vis spectroscopy within the wavelength range of 350–800 nm.

As shown in Figure 8(a), all grown samples showed strong absorption in the UV spectrum, which can be attributed to the high optical quality of the grown ZnO NRs. The absorbance capability of the undoped ZnO NRs reduced significantly in the visible light. The Cu-doped ZnO revealed relatively higher absorptions and lower transmittances in all regions than the undoped ZnO. This result can be due to the large defect that increased the absorption in the visible region and reduced the transmittance. The variation in doping concentration significantly affected the optical property of the ZnO NRs. These characteristics indicated that Cu doping of the ZnO NRs enlarged their absorption capability to a visible wavelength range, which further improved their photocatalytic activity.

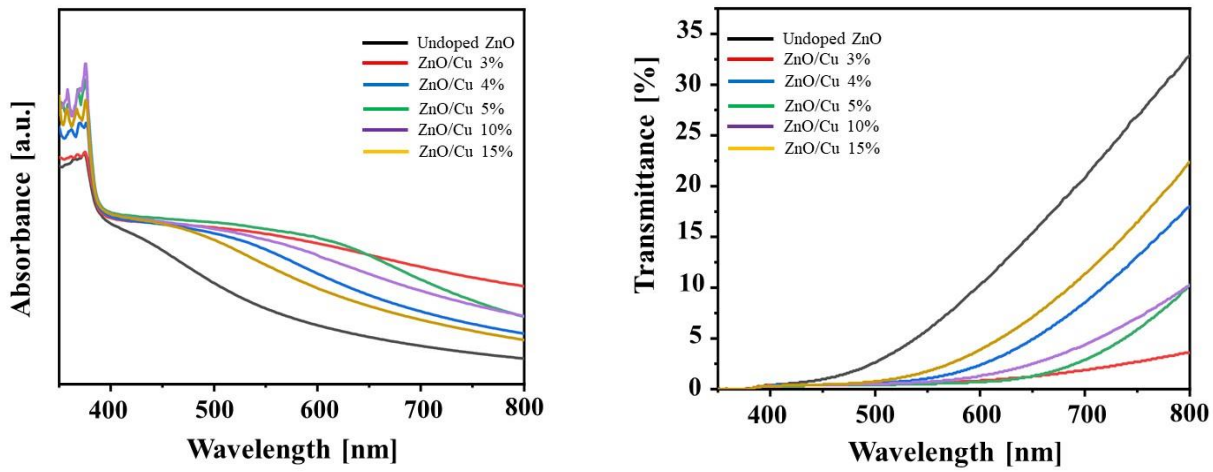

Figure 8. UV-Vis spectral analysis, (a) Absorbance and (b) transmittance of undoped ZnO nanorods, Cu concentrations of 3, 4, 5, 10, and 15 mol% at 6 h growth time.

Figure 9(a) shows the bandgap value of ZnO measured using UV-Vis spectrum analyzer and further calculated using Tauc plot (absorption versus energy) to obtain the energy gap value [71].

$$(\alpha h\nu)2 = A(h\nu\text{-}Eg)n \quad (5)$$

where α is the absorption coefficient of the material, hν is the photon energy, Eg the optical band gap, and n= 1 for direct transition and is a constant.

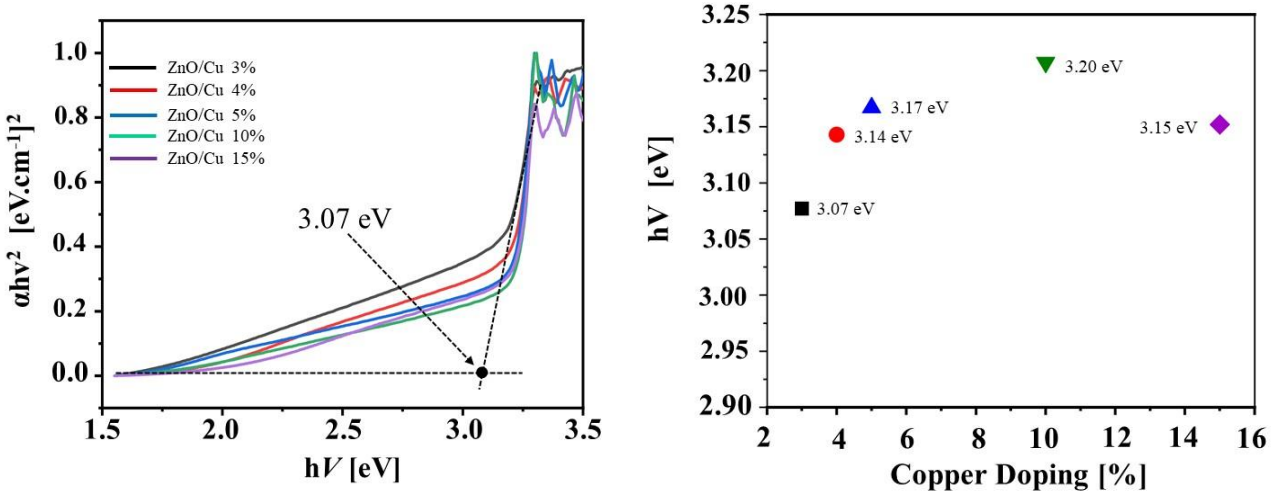

Figure 9. UV Vis spectrum analysis, (a) Tauc plot of various Cu-doped ZnO materials, (b) Analysis of energy gap ZnO nanorods with various copper doping contents in the precursor solution.

Analysis using Tauc plot agrees with the report of Beura et al. [72] about the two ways of bandgap reduction, namely, quantum size effect and electronic structure modifications. Therefore, Cu doping on ZnO is expected to modify the electronic structure of ZnO NRs and reduce its bandgap value, as shown in Figure 9(b). The bandgap energies estimated from the Tauc plot show that the Eg of the Cu-doped ZnO was approximately 3.07 eV, which was lower than the value reported previously [34, 58]. The bandgap can be reduced by decreasing Cu doping content.

3.5. Photodegradation Test

A photodegradation test of MB dyes under UV radiation was performed with the applied power of a UV lamp of 18 W for 3 h irradiation to study the photocatalytic activity of the synthesized NRs. The MB photodegradation test results were then analyzed using UV-Vis spectroscopy at the wavelength range of 300–750 nm.

The photodegradation test was run for three cycles. The three-cycle test aimed to observe the recyclability of ZnO NRs and to measure the photocatalyst degradation capability. The initial sample was the MB solution without photocatalyst, and other samples included the undoped ZnO and doped ZnO with all studied Cu compositions in the precursor. The photodegradation efficiency of the ZnO NR photocatalyst was calculated using the following equation [73]:

$$\text{Degradation } (\%) = \frac{C_0 - C}{C_0} \text{ X } 100, \quad (6)$$

where C_0 represents the initial concentration of MB before irradiation with the ZnO NR photocatalyst and C describes the concentration of MB after irradiation. Figure 10 shows the UV-Vis analysis for the photodegradation test of the MB solution tested in multiple cycles: 1st cycle (Figure 10(a)), 2nd cycle (Figure 10(b)), and 3rd cycle (Figure 10(c)). In general, all samples containing Cu-doped ZnO NRs revealed better photodegradation performance than the pristine ZnO NRs. The capability of the photocatalyst to degrade MB decreased after the third cycle. This result can be ascribed to the fact that the MB attached permanently in the ZnO NRs after the first cycle, even after flushing the chamber with DI water. This condition prevented the light from reaching the ZnO NRs, hence reducing the photocatalytic activity. Moreover, ZnO with 4 mol% Cu in the precursor revealed the highest degradation of MB concentration in the solution.

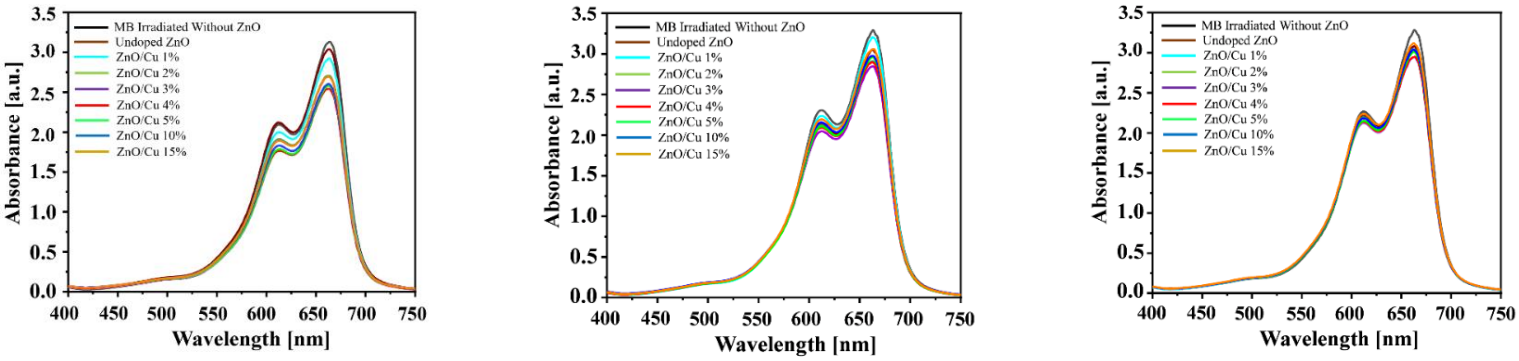

Figure 10. Photodegradation test of MB irradiated without catalyst, pristine ZnO, and doped ZnO with Cu contents of 1%, 2%, 3%, 4%, 5%, 10%, and 15% in the precursor solution in multiple cycles: (a) 1st cycle, (b) 2nd cycle, (c) and 3rd cycle.

Observation on long-term photocatalytic process (for 14 h) showed that Cu-doped ZnO showed much better performance on MB degradation with prolonged irradiation time, as shown in Figure 11(a). Figure 11(b) shows the kinetic degradation k of MB after the photocatalytic process with the ZnO/Cu NRs for 3 h to 14 h of the duration test. The k value was calculated as previously described to analyze how fast the contaminants can be reduced [74]. All samples of ZnO with Cu doping produced a better MB degradation rate higher than 0.035 k min^{-1}. The k value increased with the Cu composition, reached the maximum value at the Cu composition of 4%, then decreased with as Cu composition was further increased.

After multiple tests and a long-term photocatalysis process, a MB degradation rate of 35% was obtained by sample ZnO with 4 mol% Cu in the precursor solution, as shown in Figure 11(c). At the end of the functionality test, the samples were exposed with a high UV light intensity of 30 W. The results showed that the intensity significantly affected the degradation process. An increase in degradation rate of 177% was obtained with the maximum degradation rate of 97%, which is higher than the performance of the ZnO NP photocatalyst [19].

To analyze the stability of the ZnO/Cu catalyst after the degradation test of MB, the material properties of the multicycle tested sample were then analyzed. Figure 12 provides the XRD result of the undoped ZnO NR and Cu-doped ZnO after three-time recycling photodegradation test and their comparison with the initial ZnO/Cu photocatalyst (before the test). The crystal structure of the ZnO NRs was not affected after immersion in organic contaminants and after exposure to UV light for 3 h. The main peak intensity of the samples at (1 0 0), (1 0 2), (1 0 1), (1 0 2), and (1 0 3) remained the same. However, the main peak intensity at (0 0 2) was reduced after multiple degradation processes. This result may be attributed to the attachment of MB on the photocatalyst surface.

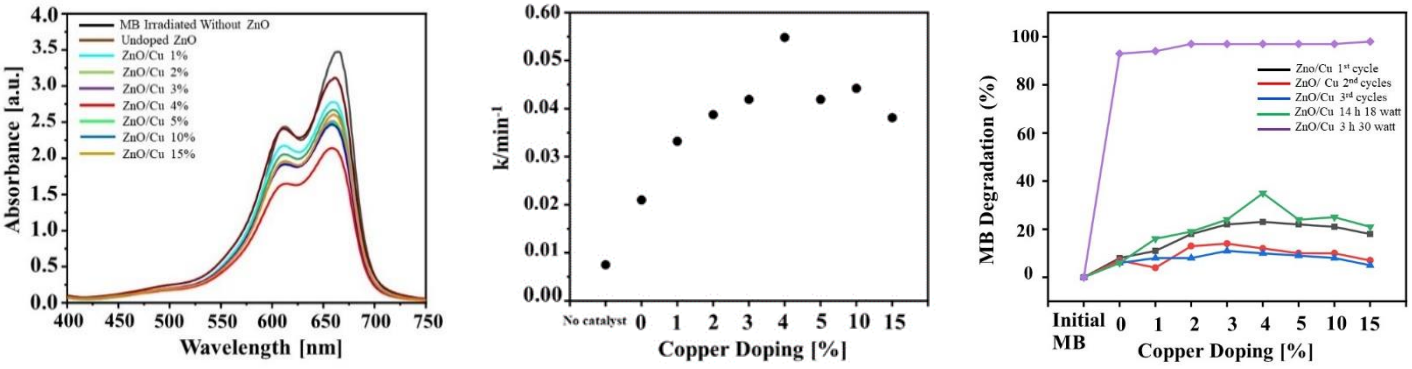

(a) (b) (c)

Figure 11. Stability test of MB degradation, (a) Irradiated without catalyst, pristine Zn, ZnO with Cu contents of 1, 2, 3, 4, 5, 10, and 15 mol% grown for 14 h, (b) Kinetic degradation k of MB after photocatalytic process with ZnO/Cu NRs for 3 h to 14 h of duration test (c) Photocatalytic performances of ZnO/Cu NRs for MB degradation after three cycling tests for 3 and 14 h and photodegradation test under 30 W UV exposure.

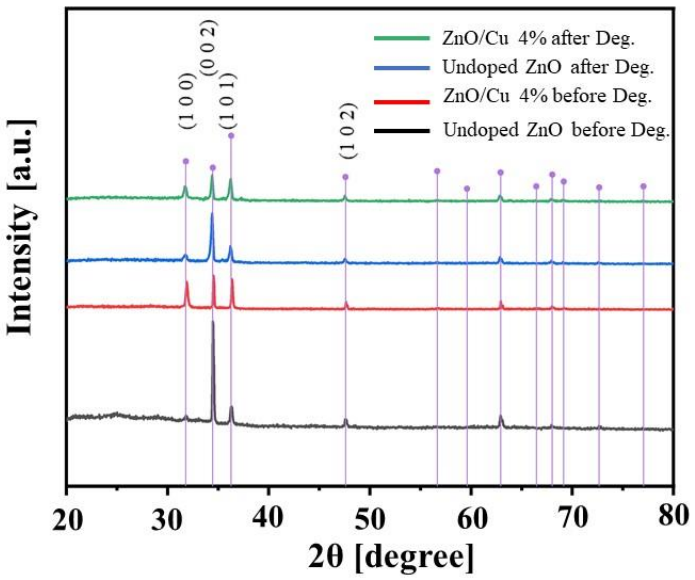

s

Figure 12. XRD results of undoped ZnO nanorods and 4 mol% Cu-doped ZnO before and after three cycling degradation processes.

4. CONCLUSION

Vertically aligned ZnO-based NRs were successfully prepared using a hydrothermal method. The synthesized material incorporated the copper doping that is aimed to enhance the photocatalytic activity. The initial process attempts of pristine ZnO showed that the NR length and diameter increased with the growth duration. Maximum rod's length and diameter of approximately 3028 and 65 nm, respectively, were obtained after 6 h growth. Typical hexagonal structures of ZnO NRs were obtained,

as shown by FESEM images. The Cu-doped ZnO had 44% shorter length and approximately 36% higher diameter than pristine ZnO. The EDAX and XRD analyses confirmed the presence of Zn, O, and Cu in the grown NR samples. The addition of Cu doping enlarged the light absorption in the visible light spectrum. Moreover, the bandgap energies estimated from the Tauc plots showed that Cu doping reduced the bandgap. UV-Vis analysis on the degradation of the MV dyes in solution illuminated under UV light showed that the reduction of the MB dyes of approximately 35% had been shown by the ZnO doped with 4 mol% Cu for 6 h. By increasing the intensity power, a maximum reduction of MB of 97% could be obtained. Therefore, Cu doping on ZnO significantly enhanced the photocatalytic activity of the ZnO-based NRs and improved the degradation of organic contamination of industrial wastewater. The developed material may be commercialized for the treatment of textile and food industry waste products, which would benefit human health and improve environmental quality.

ACKNOWLEDGMENTS
This work was supported by Universiti Kebangsaan Malaysia under Project PRGS/2/2020/TK05/UKM/01/1. and Universitas Pendidikan Indonesia under project WCP grant 2817/E4.1/KK.04.05/2021.

References

1. M. Hassaan, M. El Katory, R.M. Ali and A. El Nemr, *Egypt J Chem*, 63 (2020) 1443.
2. N. Tüfekci, N. Sivri, İ. Toroz,. *Turkish J. Fish. Aquat. Sci*., 7 (2007)
3. D. Kwon, J. Kim, *J. Nanosci. Nanotechnol*, 20 (2020) 5604.
4. A. Ghaly, R. Ananthashankar, M. Alhattab, V. V Ramakrishnan, *Chem. Eng. Process*, 5 (2014) 1.
5. M. Mekuyie, *J. Nat. Sci. Res*, 4 (2014) 47.
6. S. Ravulapalli and R. Kunta, *J. Environ. Chem. Eng*, 6 (2018) 4298.
7. K. Gong, Q. Hu, L. Yao, M. Li, D. Sun, Q. Shao, B. Qiu, Z. Guo, *J. Environ. Chem. Eng*., 6 (2018) 7283.
8. H. Peng, J. Guo, *Environ. Chem. Lett*, (2020) 1.
9. J. Dotto, M. R. Fagundes-Klen, M.T. Veit, S.M. Palacio, R. Bergamasco,*J. Clean. Prod*, 208 (2019) 656.
10. M. Byambaa, E. Dolgor, K. Shiomori, Y. Suzuki, *J. Environ. Sci. Technol*, 11 (2018) 1.
11. D. B. Miklos, C. Remy, M. Jekel, K. G. Linden, J. E. Drewes, U Hübner, *Water Res*, 139 (2018) 118.
12. G. K. Upadhyay, J. K. Rajput, T. K. Pathak, V. Kumar, L. Purohit, *Vacuum*, 160 (2019) 154.
13. J. Lin, Z. Luo, J. Liu, P. Li, *Mater. Sci. Semicond. Process*., 87 (2018) 24.
14. C. Hitam, A. Jalil, *J. Environ. Manage*, 258 (2020) 110050.
15. A. B. D. Nandiyanto, R. Ragadhita, J. Yunas, *Sains Malays*, 49 (2020) 2881.
16. S. H. Hsieh, J. M. Ting, *Appl. Surf. Sci*, 427 (2018) 465.
17. Ü. Özgür, Y. I. Alivov, C. Liu, A. Teke, M. Reshchikov, S. Doğan, V. Avrutin, S. J. Cho, H. Morkoç, *J. Appl. Phys*, 98 (2005) 11.
18. K. A. Isai, V. S Shrivastava, *Appl. Sci*, 1 (2019) 1.
19. D. Smazna, S. Shree, O. Polonskyi, S. Lamaka, M. Baum, M. Zheludkevich, F. Faupel, R. Adelung, Y. K Mishra, *J. Environ. Chem. Eng*, 7 (2019) 103016.
20. I. Kazeminezhad, A Sadollahkhani,*J. Mater. Sci.: Mater. Electron*, 27 (2016) 4206.
21. I. Khan, K. Saeed, I. Khan, *Arab. J. Chem*, 12 (2019) 908.
22. G. Singh, J. Singh, S.S. Jolly, R. Rawat, D. Kukkar, S. Kumar, S. Basu, M. Rawat, *J. Mater. Sci*. Mater, 29 (2018) 7364.
23. J. Zhang, W. Guo, Q. Li, Z. Wang, S. Liu, *Environ. Sci. Nano*, 5 (2018) 2482.

24. C. B. Ong, L.Y. Ng, A.W. Mohammad, *Renew. Sustain. Energy Rev*, 81 (2018) 536.
25. H. Wang, X. Liu, S. Han, *CrystEngComm*, 18 (2016) 1933.
26. C. Yu, K. Yang, Y. Xie, Q. Fan, C.Y. Jimmy, Q. Shu, C. Wang, *Nanoscale*, 5 (2013) 2142.
27. U. Alam, A. Khan, D. Ali, D. Bahnemann, M. Muneer, *RSC Adv.* , 8 (2018) 17582.
28. I. Iwantono, F. Anggelina, S. K. Md Saad, M. Y. A. Rahman, A. A Umar, *Mater. Express*., 7 (2017) 312.
29. S. K. Md Saad, A. Ali Umar, M. I. Ali Umar, M. Tomitori, M. Y. Abd. Rahman, M. Mat Salleh, M. oyama, *ACS omega*, 3 (2018) 2579.
30. I. Iwantono, S. K. M. Saad, R. Yuda, M. Y. Abd Rahman, A. A. Umar , *Superlattices Microstruct*., 123 (2018) 119.
31. I. Iwantono, S. K. M. Saad, F. Anggelina, A. Awitdrus, M. A. Ramli, A. A. Umar, *Phys. E: Low-Dimens. Syst. Nanostructures*, 111 (2019) 44.
32. J. Kazmi, P. C. Ooi, B. T. Goh, M. K. Lee, M. M. R. Wee, S. S. A. Karim, S. R. A. Raza, M.A.Mohamed, *RSC Adv*,10 (2020) 23297.
33. A. Shafura, N. M. Sin, M. Mamat, M. Uzer, A. Mohamad, M. Rusop, Structural properties of Al-doped ZnO thin films deposited by Sol-Gel spin-coating method, RSM 2013 IEEE Regional Symposium on Micro and Nanoelectronics, IEEE, 2013, pp. 308-311.
34. M. Rabbani, J. Shokraiyan, R. Rahimi, R. Amrollahi, *Water Sci. Technol*, 84 (2021) 1813.
35. R. S. Mohar, I. Sugihartono, V. Fauzia, A. A.Umar, *Surf. Interfaces*, 19 (2020) 100518.
36. S. Zhao, Y. Shen, X. Yan, P. Zhou, Y. Yin, R. Lu, C. Han, B. Cui, D. Wei, *Sens. Actuators B: Chem*, 286 (2019) 501.
37. D. K. Kwon, Y. Porte, J. M. Myoung, *J. Phys. Chem*. C, 122 (2018) 11993.
38. A. Saboor, S. M. Shah, H. Hussain, *Mater. Sci. Semicond. Process*, 93 (2019) 215.
39. R. Pandey, N. P. Maria Joseph Raj, V. Singh, P. Iyamperumal Anand, S.J. Kim, *ACS Appl. Mater. Interfaces.*, 11 (2019) 6078.
40. S.S.A. Karim, C.-F. Dee, B.Y. Majlis, M.A. Mohamed, *Sains Malays*, 48 (2019) 1301.
41. N. Hao, M. Zhang, J. X. J. Zhang, *Biomater. Sci*, 8 (2020) 1783.
42. M. Sajjad, I. Ullah, M. Khan, J. Khan, M. Y. Khan, M. T. Qureshi, *Results Phys*, 9 (2018) 1301.
43. S. Muthukumaran, R. Gopalakrishnan, *Opt. Mater*,. 34 (2012) 1946.
44. C.-L. Hsu, Y.-D. Gao, Y.-S. Chen, T.J. Hsueh, *ACS Appl. Mater. Interfaces*, 6 (2014) 4277.
45. Y. Wang, Y. Han, J. Han, X. Zhang, Y. Chen, S. Wang, L. Wen, N. Liu, J. Su, L. Li,Y. Gao, *Opt. Express*, 24 (2016) 3940.
46. M. Babikier, D. Wang, J. Wang, Q. Li, J. Sun, Y. Yan, Q. Yu, S. Jiao, *Nanoscale Res. Lett*., 9 (2014) 1.
47. S.-S. Xu, H.-L. Lu, Y. Zhang, T. Wang, Y. Geng, W. Huang, S.-J. Ding, D.W. Zhang *J. Alloys Compd*., 638 (2015) 133.
48. N. Mufti, I. K. Laila, R. Idiawati, A. Fuad, A. Hidayat, A. Taufiq, The effect of growth temperature on the characteristics of ZnO Nanorods and its optical properties, *Journal of Physics: Conference Series, IOP Publishing*, 2018, pp. 012005.
49. A. A. M. Raub, J. Yunas, M. A. Mohamed, J. Kazmi, J. Ridwan, Structural and Optical Properties Investigation of Graphene Oxide coated ZnO nanorods for Enhanced Photocatalytic Effect, 2021 IEEE Regional Symposium on Micro and Nanoelectronics (RSM), IEEE, 2021, pp. 104.
50. J. Ridwan, J. Yunas, A. A. Umar, A. A. M. Raub, Hydrothermal Grow of Cu doped ZnO Nanorods for Large Spectrum Photocatalyst, 2021 IEEE Regional Symposium on Micro and Nanoelectronics (RSM), IEEE, 2021, pp. 108-111.
51. S. Abrahams, J. Bernstein, *Acta Crystallogr*, 25 (1969) 1233.
52. A. Gnanaprakasam, V. Sivakumar, M. J. Thirumarimurugan, *Indian J. Eng. Mater. Sci*, 2015 (2015)
53. T. Soltani, M. H. Entezari, *J. Chem. Eng*, 223 (2013) 145.
54. Y. R. Uhm, B. Sun Han, C.K. Rhee, S. J. Choi, *J. Nanomater*, 2013 (2013)
55. A. K. Singh, G. S. Thool, R. Singh, S.P. Singh, *J. Alloys Compd*, 618 (2015) 421.

56. R. Shabannia, *J. Mol. Struct*, 1118 (2016) 157.
57. T. C. Damen, S. Porto, B. Tell, *Physical Review* E, 142 (1966) 570.
58. A. F. Abdulrahman, S.M. Ahmed, N. M. Ahmed, M. A. Almessiere, Fabrication, characterization of ZnO nanorods on the flexible substrate (Kapton tape) via chemical bath deposition for UV photodetector applications, AIP Conference Proceedings, AIP Publishing LLC, 2017, pp. 020004.
59. V. I. Korepanov, S.Y. Chan, H. C. Hsu, H.o. Hamaguchi, Heliyon, 5 (2019) e01222.
60. I. Campbell, P. M. Fauchet, *Solid State Commun*, 58 (1986) 739.
61. N. D. Raskar, D. V. Dake, V. A. Mane, E. Stathatos, U. Deshpande, B. Dole, *J. Mater. Sci. Mater. Electron*, 30 (2019) 10886.
62. A. Aravind, M. Jayaraj, M. Kumar, R. Chandra, *J. Mater. Sci. Mater. Electron*, 24 (2013) 106.
63. L. Chow, O. Lupan, G. Chai, H. Khallaf, L. K. Ono, B. R. Cuenya, I. Tiginyanu, V. V. Ursaki, V. Sontea, A. Schulte, *Sens. Actuator A Phys*, 189 (2013) 399.
64. L.B. Saad, L. Soltane, F. Sediri, *Russ. J. Phys. Chem*. A, 93 (2019) 2782.
65. H. He, Q. Yang, C. Liu, L. Sun, Z. Ye, *J. Phys. Chem*. C, 115 (2011) 58.
66. A. Galdámez-Martinez, G. Santana, F. Güell, P.R. Martínez-Alanis, A. Dutt, *J. Nanomater*, 10 (2020) 857.
67. Q. Jiang, Z.Y. Wu, Y.M. Wang, Y. Cao, C.F. Zhou, J.H. Zhu, *J. Mater. Chem*, 16 (2006) 1536.
68. S.C. Choi, D.K. Lee, S.H. Sohn, *J. Catal*, 10 (2020) 614.
69. R. Raji, K. Gopchandran, *Mater. Res. Express*, 4 (2017) 025002.
70. L. Saikia, D. Bhuyan, M. Saikia, B. Malakar, D.K. Dutta, P. Sengupta, *Appl. Catal. A: Gen*, 490 (2015) 42.
71. J. Tauc, R. Grigorovici, A. Vancu, *Phys. Status Solidi* B, 15 (1966) 627.
72. A. Gaurav, R. Beura, J.S. Kumar, P. Thangadurai, *Mater. Chem. Phys*, 230 (2019) 162.
73. A. Ramos-Corona, R. Rangel, J. Alvarado-Gil, P. Bartolo-Pérez, P. Quintana, G. Rodríguez-Gattorno, *Chemosphere*, 236 (2019) 124368.
74. D. Wibowo, M. Z. Muzakkar, S. K. M. Saad, F. Mustapa, M. Maulidiyah, M. Nurdin, A.A. Umar, *J. Photochem. Photobiol*. A, 398 (2020) 112589.